Catalysis Today 429 (2024) 114508

Contents lists available at ScienceDirect

Catalysis Today

journal homepage: www.elsevier.com/locate/cattod

Silica as support and binder in bifunctional catalysts with ultralow Pt loadings for the hydroconversion of *n*-alkanes

Luc C.J. Smulders [a], Arvid J. Beeuwkes [a], Kang Cheng [a], Johannes D. Meeldijk [a,b], Zhuoran Xu [c], George F. Tierney [a], Eric Doskocil [c], S. Tegan Roberts [d], Glenn J. Sunley [d], Petra E. de Jongh [a], Krijn P. de Jong [a,*]

[a] Materials Chemistry and Catalysis, Debye Institute for Nanomaterials Science, Utrecht University, Universiteitsweg 99, 3584 CG Utrecht, the Netherlands
[b] Electron Microscopy Centre, Utrecht University, Universiteitsweg 99, 3584 CG Utrecht, the Netherlands
[c] Applied Sciences, bp Innovation & Engineering, BP Products North America Inc., 30 S. Wacker Dr, Chicago, IL 60606, United States
[d] Applied Sciences, bp Innovation & Engineering, BP plc, Saltend, Hull HU12 8DS, United Kingdom

ARTICLE INFO

Keywords:
Bifunctional catalysis
Hydroconversion
Silica
Zeolites
Platinum

ABSTRACT

Hydroconversion is a key step in the production of ultraclean fuels from renewable sources. This reaction is carried out using a bifunctional catalyst consisting of a base metal sulfide or a noble metal and a solid acid. Recently, we have shown that for Pt/Al_2O_3/ZSM-22 catalysts with low Pt loadings ($\leq$0.01 wt%) it is advantageous – to both the activity as well as the isomer selectivity - to emplace the Pt on the zeolite crystallites instead of on the Al_2O_3 binder. When these low loadings of Pt were on the alumina binder, small clusters or even single atoms were present which were hard to reduce leading to inactivity of the catalysts. Herein, we explore the replacement of alumina by silica, and the performance of catalysts with ultralow Pt loadings on the conversion of longer-chain hydrocarbons. A series of Pt/SiO_2/ZSM-22 catalysts with varying Pt weight loadings (0.001, 0.005, 0.01, 0.05, 0.1 and 0.5 wt%) and location (on silica or on ZSM-22) was prepared and characterized using ICP, NH_3-TPD, HAADF-STEM and XAS. Their hydroconversion performance was evaluated using *n*-heptane and *n*-hexadecane as model feedstocks. As for the Pt/Al_2O_3/ZSM-22 catalysts systems, for Pt/SiO_2/ZSM-22 catalysts with low Pt loadings ($\leq$0.01 wt% for *n*-heptane conversion) it was beneficial to have the Pt nanoparticles on the ZSM-22 crystals. Hydroconversion of *n*-hexadecane over Pt/SiO_2/ZSM-22 and Pt/Al_2O_3/ZSM-22 catalysts showed that for feedstocks with a higher molecular weight, higher Pt loadings ($\geq$0.05 wt%) are required for sufficient catalytic performance. For the conversion of *n*-hexadecane it was beneficial to locate these higher amounts of Pt on the binder.

1. Introduction

Platinum group metals (PGMs) are indispensable for several emerging and established technologies. Platinum, for example, is utilized in fuel cells [1,2], electrolyzers [3], catalytic converters [4], and refinery catalysts [5]. Although their applicability is large, their reserves are not and supply of PGMs is considered to be at risk [6,7]. Therefore, it is necessary to look into ways to improve recycling and to maximize their utilization.

One refinery process requiring PGMs is the hydroconversion of alkane feedstocks. This is a key step in the production of ultraclean fuels and lubricants from renewable sources, such as Fischer–Tropsch waxes [8,9], biobased fatty acids [10], or plastic waste [11–13]. Hydroconversion is performed with a bifunctional catalyst consisting of a metal (sulfide) function and an acid function, for dehydrogenation-hydrogenation and isomerization-cracking, respectively [14,15]. These roles are typically fulfilled by base metal sulfides or Pt, in combination with amorphous silica-aluminas, zeolites, or zeotypes [16]. Previous research regarding hydroconversion focused on the ideal distance between these two functions [17–20], and their respective ratio, known as the metal-to-acid-site (n_M/n_A) ratio. [21–23].

To optimize PGM utilization in hydroconversion catalysts, we previously studied the optimal Pt weight loading as a function of the Pt location [24]. At regular weight loadings of 0.1–0.5 wt%, it is beneficial to have the metal function on the alumina binder, at nanoscale distance from the zeolite acid sites [19,24–27]. However, for Pt/Al_2O_3/ZSM-22

* Corresponding author.
E-mail address: k.p.dejong@uu.nl (K.P. de Jong).

https://doi.org/10.1016/j.cattod.2024.114508
Received 22 August 2023; Received in revised form 30 November 2023; Accepted 2 January 2024
Available online 5 January 2024

catalysts the loading could be reduced to 0.01 wt% Pt when the Pt nanoparticles were placed on the zeolite crystals, without compromising catalytic activity, selectivity towards isomers, or stability during the hydroconversion of *n*-heptane. For hydroconversion of longer chain hydrocarbons, e.g. *n*-hexadecane, the n_M/n_A ratio has to be higher for an optimal performance [28,29]. Although the reactivity of these longer hydrocarbons differs from the shorter ones [29–31], optimal Pt weight loading as function of the Pt location has not been studied for feedstocks with higher molecular weight yet.

Additionally, characterization of the low (0.01 wt% Pt) loaded catalysts in our previous study [24] – after reduction – revealed the presence of Pt-O species when Pt was on the alumina binder. These Pt-O species are most probably inactive as (de)hydrogenation catalysts. This was confirmed by the assessment of the performance of bifunctional catalysts containing Pt single atoms. It was concluded that reduced Pt nanoparticles are required for (de)hydrogenation and hence hydroconversion activity.

Another, albeit less often utilized inorganic binder is silica. It is used in both industrial and academic research [32–36]. Although extrudates prepared with silica have been shown to undergo solid ion exchange, decreasing the Brønsted acidity of the zeolites [37–39], silica is also known to aid in the retainment of zeolite structural stability [40]. Another possible advantage is that metal nanoparticles supported on silica are typically more readily reduced than nanoparticles of the same composition on alumina [41,42].

In this work, we explored the replacement of the alumina binder material by a silica binder material and we assess the optimal Pt location for the conversion of longer chain hydrocarbons when ultralow Pt loadings are used.

2. Materials and methods

2.1. Materials

ZSM-22 (H^+-form, SiAl = 32.5–40 at/at) was purchased from ACS Material. Aerosil 380 silica was purchased from Evonik. Boehmite (70 wt% Al_2O_3) was supplied by Shell Technology. Tetraamine platinum (II) nitrate ($Pt(NH_3)_4(NO_3)_2$, 99.995% pure), chloroplatinic acid ($H_2PtCl_6{\cdot}6H_2O$, ≥37.5 wt% Pt) and acetic acid were purchased from Sigma-Aldrich. *n*-Heptane (99+%, pure) and *n*-hexadecane (99%, pure) were obtained from ACROS Organics. Ammonia solution (NH_4OH, 25%) was obtained from Emsure. Silicon carbide (SiC, SIKA ABR I F70, grain size: 220 μm) was supplied by Fiven. H_2 6.0, He 5.0 and N_2 5.0, were obtained from Linde gas.

2.2. Catalyst preparation

2.2.1. Preparation of Pt/SiO_2/ZSM-22 catalysts

ZSM-22 was calcined in a flow of synthetic air (N_2/O_2, 80/20, *vol/vol*) at 500 °C (ramp 5 °C min^{-1}) for 5 h. Solutions containing 6.0 mM and 0.6 mM of tetraamine platinum nitrate (PTA) were prepared by dissolving in Milli-Q water. Pt-SiO_2/ZSM-22 catalysts were prepared using an electrostatic adsorption method adapted from Regalbuto et al. [43]. 500 mg of silica was dispersed in 300 mL Milli-Q water by mechanical stirring at 400 rpm for 1 h. Subsequently, the required volume of the 6.0 mM or 0.6 mM PTA solution was further diluted with 50 mL Milli-Q water and added dropwise to the dispersion, after which the pH was increased to 7 using a 0.15 M aqueous ammonia solution. The resulting dispersion was stirred for 3 additional hours. This dispersion was then filtered over vacuum. The filter cake was dried overnight in a static oven at 120 °C. Once dried, it was crushed and transferred to a tubular reactor. The dried catalyst precursor was then calcined in a total flow of 100 mL min^{-1} of synthetic air (N_2/O_2, 80/20, *vol/vol*) at 350 °C (ramp: 0.2 °C min^{-1}) for 2 h and reduced in a H_2 rich atmosphere (H_2/N_2, 80/20, *vol/vol*) at 600 °C (ramp: 5 °C min^{-1}) for 3 h. After cooling down to room temperature the resulting powder was mixed with calcined ZSM-22. For this, the ZSM-22 was first mixed with 100 μL of a 1.5 mM aqueous ammonia solution and 250 μL Milli-Q water using a mortar and pestle for 15 min. After this the Pt/SiO_2 powder was added and mixed for an additional 15 min. The resulting paste was dried in a static oven at 120 °C overnight and calcined (N_2/O_2, 80/20, *vol/vol*) at 500 °C (ramp: 5 °C min^{-1}) for 2 h.

Pt-ZSM-22/SiO_2 catalysts were prepared via ion exchange (IE). First, 500 mg of calcined ZSM-22 was dispersed in 300 mL Milli-Q water by stirring mechanically at 400 rpm for 1 h. Meanwhile, the required volume of 6 mM PTA solution was further diluted with Milli-Q water to obtain a PTA solution of 50 mL with the desired concentration. This solution was added dropwise to the dispersion, and stirred for an additional 3 h. The dispersion was filtered over vacuum and the resulting filter cake was dried in a static oven at 120 °C overnight. The powder was then transferred to a tubular reactor and calcined in a flow (100 mL min^{-1}) of synthetic air (N_2/O_2, 80/20, *vol/vol*) at 350 °C (ramp: 0.2 °C min^{-1}) for 2 h. This was followed by reduction in a H_2 rich atmosphere (H_2/N_2, 80/20, *vol/vol*) at 600 °C (ramp: 5 °C min^{-1}) for 3 h and cooling down to room temperature. 500 mg of Aerosil 380 was then mixed with 100 μL of a 1.5 mM aqueous ammonia solution and 250 μL Milli-Q water using a mortar and pestle for 15 min, after which the Pt/ZSM-22 catalyst was added to the mortar. The powders were stirred for additional 15 min. The resulting paste was again dried in a static oven at 120 °C overnight and calcined (N_2/O_2, 80/20, *vol/vol*) at 500 °C (ramp: 5 °C min^{-1}) for 2 h.

2.2.2. Preparation of Pt/γ-Al_2O_3/ZSM-22 catalysts

Pt/γ-Al_2O_3/ZSM-22 catalysts were prepared as previously reported [24]. ZSM-22 was calcined in a flow of synthetic air (N_2/O_2, 80/20, *vol/vol*) at 500 °C for 5 h with a ramp of 1 °C min^{-1}. Zeolite-alumina composite (1/1, *wt/wt*) material was prepared by mixing using acetic acid for the deagglomeration of boehmite. In order to obtain 10 g of composite, firstly, 7.14 g of boehmite was mixed with 6 mL Milli-Q H_2O and 0.21 mL acetic acid using mortar and pestle. When wetting of the boehmite was complete, 5 g of ZSM-22 was added to the mortar. Then, the mixture was mixed for 10 min using a mortar and pestle and additional Milli-Q H_2O was added until a homogeneous paste was obtained. The resulting paste was dried overnight in an oven at 120 °C. The dried powder was crushed and calcined for 2 h at 500 °C using a ramp of 5 °C min^{-1}.

Pt-γ-Al_2O_3/ZSM-22 catalysts with varying Pt weight loadings (0.005 – 0.5 wt%) were prepared via electrostatic adsorption [24,43]. For this, 1.5 g of the composite material was dispersed in 450 mL Milli-Q H_2O and stirred for 30 min. The pH of the dispersion was adjusted to 2.6 using a 1 M aqueous solution of hydrochloric acid. At this pH value, the surface of the Al_2O_3 is positively charged. A given volume of an aqueous solution of chloroplatinic acid (0.17 mg_{Pt} mL^{-1}) was added dropwise. The dispersion was stirred for 3 h, after which it was filtered and washed with 500 mL Milli-Q H_2O. The filter cake was dried overnight in an oven at 120 °C. The resulting catalyst powder was reduced in a flow of H_2/N_2 (20/80, *vol/vol*) at 500 °C for 3 h using a heating ramp of 1 °C min^{-1} and calcined for 2 h at 500 °C in a flow of synthetic air (N_2/O_2, 80/20, *vol/vol*).

For the preparation of Pt-ZSM-22/γ-Al_2O_3, firstly, 0.75 g of ZSM-22 was dispersed in 225 mL Milli-Q H_2O and stirred for 30 min. Then a given volume of the PTA solution was added dropwise and the mixture was stirred for 3 h. The dispersion was filtered without further washing and both the filtrate and the filter cake were collected. The filter cake was dried in an oven at 60 °C and reduced (H_2/N_2, 20/80, *vol/vol*) at 500 °C for 3 h with a ramp of 1 °C min^{-1}. When cooled to room temperature the resulting powders were redispersed in the filtrate that still contained PTA. The IE procedure including stirring, filtration, drying and reduction was performed a second time. The Pt-ZSM-22/γ-Al_2O_3 composite catalyst was then prepared by mixing the Pt/ZSM-22 catalyst with boehmite, using acetic acid as peptizing agent, followed by drying and calcination as described for the preparation of ZSM-22/γ-Al_2O_3

composite, but now with a heating ramp of 1 °C min^{-1} during calcination.

2.3. Catalyst characterization

2.3.1. Quantification of metal and acid sites

Analysis of the elemental composition of the catalysts was performed at Mikroanalytisches Laboratorium Kolbe, Germany, using an inductively coupled plasma optical emission spectrometer (ICP-OES). Prior to measurements, samples were dissolved according to their standard in-house procedures.

Temperature programmed desorption of ammonia (NH_3-TPD) was performed to quantify the number of acid sites in each catalyst. The measurements were performed on a Micromeritics AutoChem II equipped with a thermal conductivity detector (TCD) calibrated for ammonia. For a typical measurement 80–110 mg of catalyst was dried in a helium flow for 1 h at 600 °C with a ramp of 10 °C min^{-1}. This was followed by lowering the temperature to 100 °C after which ammonia (10 vol% in He) was introduced in a pulse-wise manner until oversaturation was accomplished. After this, the physisorbed ammonia was removed by flushing He for 2 h at 100 °C. Subsequently, the desorption of ammonia up to 600 °C with a ramp of 10 °C min^{-1} was monitored.

2.3.2. Nitrogen physisorption

Measurements of N_2 physisorption isotherms were performed at −196 °C on a Micromeritics Tristar II Plus apparatus. Prior to the measurement, the samples were dried in a nitrogen flow at 300 °C. The accessible surface areas of the catalysts were determined with the Brunauer–Emmett–Teller (BET) method. A Harkins-Jura thickness curve fitted between 0.32 and 0.40 nm thickness was used to determine micropore (<2 nm) volumes. Total pore volumes were derived from the volume of N_2 adsorbed at $P/P_0 = 0.95$.

2.3.3. Electron microscopy

Prior to studying the samples with electron microscopy, the samples were ultramicrotomed. Firstly, the samples were embedded in EpoFix resin, and then left to harden in an oven at 60 °C overnight. To obtain slices with a thickness of 70 nm, the resin-embedded samples were cut using a Reichert–Jung Ultracut E ultramicrotome and a Diatome Ultra 35° diamond knife. The resulting sections were deposited on glow-discharged carbon-formvar-coated copper grids (200 mesh). High-resolution high-angle annular dark-field scanning transmission electron microscopy (HAADF-STEM) was performed on a Thermo Fisher Scientific Spectra 300 S/TEM operating at 300 kV. The number average particle size (d_n) of the Pt nanoparticles was determined by measuring the nanoparticle diameter using ImageJ software, followed by a calculation using Eq. (1). Furthermore, the surface average particle size (d_s) in each catalyst sample was calculated using Eq. (2).

$$d_n \pm \sigma_{dn} = \frac{1}{N}\sum_{i=1}^{N} d_i \pm \sqrt{\frac{1}{N}\sum_{i=1}^{N}(d_n - d_i)^2} \quad (1)$$

$$d_s \pm \sigma_{ds} = \frac{\sum_{i=1}^{N} d_i^3}{\sum_{i=1}^{N} d_i^2} \pm \sqrt{\frac{1}{N}\sum_{i=1}^{N}(d_s - d_i)^2} \quad (2)$$

2.3.4. X-ray absorption spectroscopy

X-ray Absorption Spectroscopy was performed at the Advanced Photon Source (APS), Argonne National Lab, USA, at the Insertion Device of sector 10. Measurements were performed at the Pt L_3 edge (11.563 keV) in fluorescence mode, using a double monochromator with direct drive air bearings and two sets of crystals: Si (111) and Si (311). To filter out the higher harmonics present in the X-ray beam, a 60 cm long flat harmonic rejection mirror was used. Approximately 100 mg of sample was pressed into a pellet and placed in a sample holder at 45° to the beam direction. The holder was placed in an in situ temperature programmable sample cell operated under ambient pressure. The samples were reduced for 1 h in a gas flow of 100 mL min^{-1} containing 3.5 vol% H_2/He at 400 °C, after which they were cooled to room temperature. Fluorescence data were collected with an ion chamber Lytle detector with a step size of 0.5 eV and an acquisition time of 0.1 s per point. XANES spectra were processed using Athena software (Demeter 0.9.26) by averaging 12 scans for each sample [44,45]. For the 0.01Pt-SiO_2/ZSM-22 sample 58 scans were averaged to improve the low Pt signal/noise. Normalization of the XANES data was done by dividing the absorption intensities by the height of the absorption edge and subtracting the background using cubic spline routines. The oxidation state of Pt was determined from Linear Combination Fitting (LCF) from Athena in the derivative space of μ(E). For this, PtO_2 $Pt(NH_3)_4(NO_3)_2$ and Pt foil were used as reference standards for Pt^{4+}, Pt^{2+} and Pt^0, respectively. The data was fitted to the references in the range of 20 eV below and 30 eV above the Pt L_3 edge energy. EXAFS fitting was performed by converting the spectra in *k*-space with *k*-weight 2 and in the range of 2.0–11 $Å^{-1}$, d_k of 0.5, R range of 1.3–3.0 Å, d_r of 0.5, and a Hanning window. Multiple shell fitting was performed involving Pt-Pt and Pt-O paths in R space. Data for back scattering amplitudes were obtained with the built-in FEFFIT calculation using the Artemis software [45]. Prior to fitting of the acquired EXAFS data, the amplitude reduction factor (S_0^2) was calculated by fitting a Pt^0 reference foil using a Pt FCC.*cif* file taken from an online source (Materials Project, mp-126), yielding a value of 0.7 applied to all fitted Pt L_3 edge datasets.

2.4. Hydroconversion of n-heptane and n-hexadecane

The hydroconversion performance of the catalysts was assessed using an Avantium Flowrence 16 parallel fixed bed reactor setup with *n*-heptane (*n*-C7) and *n*-hexadecane (*n*-C16) as feedstock. Stainless steel reactors (inner diameter = 2 mm) were loaded with SiC (220 μm) until it reached a bed height of 2 cm. On top of this SiC bed, 30 mg of sieved catalyst (75–212 μm) was loaded. This was followed by adding more of the SiC, leaving 2 cm of free space at the top of the reactor. Analysis of the products was performed using an online GC (Agilent Technologies 7890B) equipped with an Agilent J&W HP-PONA column. The hydrocarbon products were analyzed using an FID. Prior to the catalytic tests with *n*-heptane the catalysts were reduced in H_2/He (90 vol% H_2) at 400 °C for 2 h. When *n*-hexadecane was studied, activation was caried out in pure H_2 at 400 °C for 3 h. Experiments with *n*-heptane feedstock were performed with the following reaction conditions: H_2/*n*-heptane molar ratio of 10, total pressure of 10 bar and WHSV of 2.4 $g_{n\text{-}C7}\cdot g_{cat}^{-1}\cdot h^{-1}$. When *n*-hexadecane was used as a feedstock, the following reactions conditions were applied: H_2/*n*-hexadecane molar ratio of 10, total pressure of 5 bar and WHSV of 2.9 $g_{n\text{-}C16}\cdot g_{cat}^{-1}\cdot h^{-1}$. These pressures were chosen to prevent alkane condensation during reaction.

The conversion of *n*-heptane or *n*-hexadecane ($X_{n\text{-alkane}}$) was calculated using:

$$X_{n\text{-alkane}} = \left(1 - \frac{F_{Cwt.n-alkane,out}}{F_{Cwt.n-alkane,in}}\right) \bullet 100\% \quad (3)$$

Where $F_{Cwt.n\text{-alkane,out}}$ and $F_{Cwt.n\text{-alkane,in}}$ are the flows based on carbon weight of *n*-alkane going out or in the reactor, respectively. The isomer yield ($Y_{i\text{-alkane}}$) was calculated using:

$$Y_{i-alkane} = \left(\frac{F_{Cwt.i-alkane,out}}{F_{Cwt.n-alkane,in}}\right) \bullet 100\% \quad (4)$$

Similarly, the yield of any cracked product was calculated using:

$$Y_{Cm} = \left(\frac{F_{Cwt.Cm,out}}{F_{Cwt.n-alkane,in}}\right) \bullet 100\% \quad (5)$$

In which Cm is a hydrocarbon molecule with m carbon atoms (m = 1–6 during *n*-heptane conversion and m = 1–14 during *n*-hexadecane conversion).

For *n*-hexadecane, the yield in mol-% of a product with m carbon

atoms was calculated as follows:

$$Y_{\mathrm{Cm}}\ (mol-\%) = \left(\frac{F_{C\mathrm{wt.Cm,out}}}{F_{\mathrm{Cwt.}n-\mathrm{alkane,in}}}\right) \bullet \left(\frac{16}{m}\right) \bullet 100\% \quad (6)$$

The selectivity towards *i*-heptane (*i*-C7), *i*-hexadecane (*i*-C16), or cracked products (Cm) during hydroconversion was calculated with the following two equations:

$$S_{i-\mathrm{C7}} = \left(\frac{F_{\mathrm{Cwt.}i-\mathrm{C7,out}}}{F_{\mathrm{Cwt.}n-\mathrm{alkane,in}} - F_{\mathrm{Cwt.}n-\mathrm{alkane,out}}}\right) \bullet 100\% \quad (7)$$

$$S_{i-\mathrm{C16}} = \left(\frac{F_{\mathrm{Cwt.}i-\mathrm{C16,out}}}{F_{\mathrm{Cwt.}n-\mathrm{alkane,in}} - F_{\mathrm{Cwt.}n-\mathrm{alkane,out}}}\right) \bullet 100\% \quad (8)$$

$$S_{\mathrm{Cm}} = \left(\frac{F_{C\mathrm{wt.Cm,out}}}{F_{\mathrm{Cwt.}n-\mathrm{alkane,in}} - F_{\mathrm{Cwt.}n-\mathrm{alkane,out}}}\right) \bullet 100\% \quad (9)$$

It should be noted that the C15 peaks overlap with *i*-C16 peaks in the chromatogram, and therefore it is assumed that Y_{C1} (mol-%) = Y_{C15} (mol-%). This holds when hydrogenolysis activity is low, which is the case for the Pt based catalysts. The signals for 'C15′ and *i*-C16 peaks are ascribed to *i*-C16 products.

3. Results and discussion

3.1. Quantification of metal and acid sites

The platinum weight loadings and number of acid sites are summarized in Table 1. The actual Pt weight loading was close to the intended weight loading resulting in a series of Pt-SiO_2/ZSM-22 (Pt-on-silica) and Pt-ZSM-22/SiO_2 (Pt-on-ZSM-22) catalysts with weight loadings of 0.005, 0.01, 0.05, 0.1, and 0.5 wt%. The number of acid sites as determined by temperature programmed desorption of ammonia (NH_3-TPD) was in all cases between 0.14 and 0.19 mmol g^{-1} with no clear correlation with Pt loading.

The Pt weight loadings were similar to the weight loadings on the Pt/Al_2O_3/ZSM-22 catalysts as previously reported [24]. The numbers of acid sites in the Pt/SiO_2/ZSM-22 were slightly higher compared to those of the Pt/Al_2O_3/ZSM-22 catalysts, which might have been caused by using a different batch of ZSM-22 or by effects caused by the binder [35,37]. It is not expected that these differences were caused by dealumination of the zeolite as has been observed with silica binders before [34,38], since the number of acid sites per gram of composite (50/50 zeolite/binder by mass) material was approximately half of the number of acid sites in pristine ZSM-22 (0.280 mmol g^{-1}, Table S1).

3.2. Location and size of Pt nanoparticles

The location and size of Pt nanoparticles were determined by high resolution HAADF-STEM. Prior to the measurement, most of the catalysts were ultramicrotomed to sections with a thickness of 70 nm. This allowed for looking "inside" the catalyst grains and distinguishing Pt nanoparticles on the ZSM-22 from Pt nanoparticles on the silica binder (Fig. 1). The resolution and contrast for Pt-SiO_2/ZSM-22 catalysts with a weight loading ≤0.01 wt% were not high enough to distinguish Pt nanoparticles unambiguously, due to a combination of a high Pt dispersion, ultralow Pt loadings, and the use of a resin. The 0.01Pt-SiO_2/ZSM-22 was imaged without performing ultramicrotomy, with the sample deposited onto a TEM grid by dipping the grid into a small sieve fraction (<75 μm) of the sample (Fig. 1f). This ensured the deposition of a very thin layer.

Based on the HAADF-STEM images the average Pt particle diameter was determined and the corresponding dispersion was calculated (Table 1). All samples displayed well dispersed Pt nanoparticles on either the ZSM-22, both in and on the zeolite crystals (Fig. 1a, c and e), or on the silica binder (Fig. 1b, d and f). However, in several images, a few larger Pt nanoparticles with a diameter up to 10 nm were observed as illustrated in Fig. 1c and as inferred from the standard deviations in the average Pt particle diameters (Table 1), in particular for 0.1Pt-SiO_2/ZSM-22. This may have been caused by redissolution of platinum by the NH_3 peptizing agent, followed by rapid drying and calcination of the paste. HAADF-STEM on a physical mixture of 0.4Pt/SiO_2 + ZSM-22, prepared without the use of a peptizing agent (Fig. S1), was performed to investigate the impact of the use of NH_3. The images that were obtained showed well-dispersed Pt nanoparticles, confirming that the larger Pt nanoparticles have formed in the peptizing and (re-)calcination process. During the preparation of 0.1Pt-SiO_2/ZSM-22 there might have been a temporary higher concentration of NH_3 if the additional Milli-Q water was not added immediately afterwards, causing increased redissolution leading to a larger increase of particle size compared to the other catalysts. Since the few larger particles were outnumbered by

Table 1
Results of quantification of metal and acid sites; Pt weight loading, particle size and dispersion, and number of strong acid sites.

Catalyst	Intended Pt weight loading (wt%)	Pt weight loading[a] (wt %)	Number of strong acid sites[b] (mmol g^{-1})	$d_n \pm \sigma_n$[c] (nm)	$d_s \pm \sigma_s$[d] (nm)	Dispersion[e] (%)	n_{Pt}/n_A
0.005Pt-SiO_2/ZSM-22	0.005	0.004	0.160	n.d.	n.d.	100[f]	0.001
0.01Pt-SiO_2/ZSM-22	0.01	0.012	0.139	~0.8[g]	~1.3[g]	100	0.004
0.05Pt-SiO_2/ZSM-22	0.05	0.041	0.142	1.2 ± 1.1	4.0 ± 1.6	94	0.014
0.1Pt-SiO_2/ZSM-22	0.1	0.13	0.182	2.6 ± 3.6	12.3 ± 4.5	43	0.016
0.5Pt-SiO_2/ZSM-22	0.5	0.46	0.158	1.1 ± 0.9	4.1 ± 1.5	100	0.15
0.005Pt-ZSM-22/SiO_2	0.005	0.004	0.166	1.1 ± 0.4	1.3 ± 1.1	100	0.001
0.01Pt-ZSM-22/SiO_2	0.01	0.009	0.154	0.9 ± 0.4	1.6 ± 1.0	100	0.003
0.05Pt-ZSM-22/SiO_2	0.05	0.054	0.136	1.3 ± 1.9	10.1 ± 2.3	86	0.018
0.1Pt-ZSM-22/SiO_2	0.1	0.11	0.145	1.4 ± 1.7	7.4 ± 2.3	82	0.032
0.5Pt-ZSM-22/SiO_2	0.5	0.41	0.189	1.1 ± 0.3	1.3 ± 1.2	100	0.11

[a] Determined by inductively coupled plasma optical emission spectroscopy on digested samples.
[b] Determined by deconvolution of NH_3-TPD profiles and integration of the peak at T ≥ 300 °C.
[c] Number average size of Pt nanoparticles as determined using HAADF–STEM, based on at least 150 counts.
[d] Surface average particle size as determined using HAADF–STEM followed by calculation using Eq. (2).
[e] Dispersion = $1.13/d_{Pt}$ [46]. Dispersion of Pt with d_{TEM} <1.13 nm was estimated to be 100%.
[f] Based on the absence of observable Pt nanoparticles or clusters in HAADF–STEM and the lower weight loading than the 0.01Pt-SiO_2/ZSM-22 catalyst.
[g] Average diameter of Pt nanoparticles based on 3 nanoparticles.

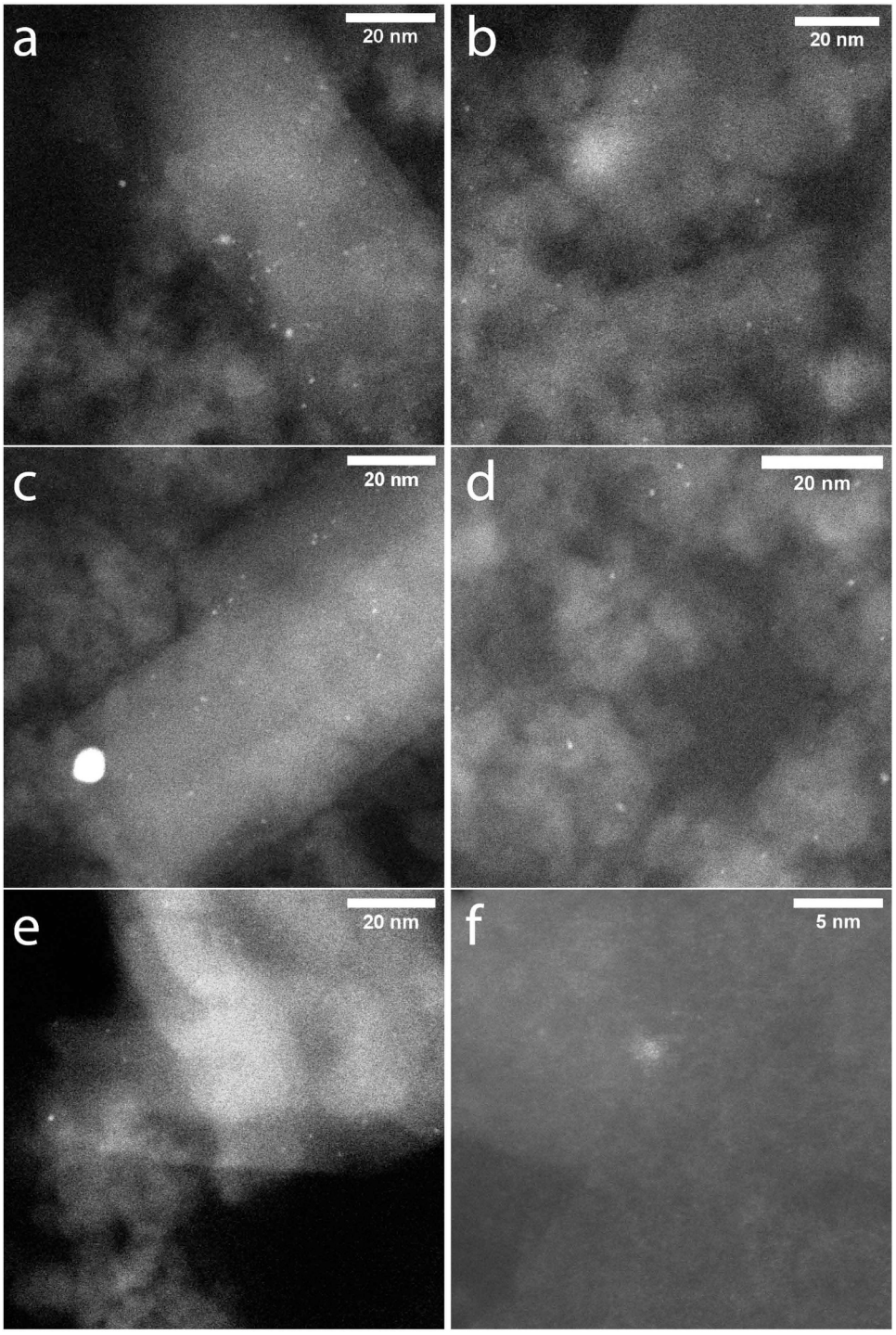

Fig. 1. HAADF STEM images of ultramicrotomed samples of (a) 0.5Pt-ZSM-22/SiO_2, (b) 0.5Pt-SiO_2/ZSM-22, (c) 0.1Pt-ZSM-22/SiO_2, (d) 0.1Pt-SiO_2/ZSM-22, (e) 0.01Pt-ZSM-22/SiO_2, (f) (not ultramicrotomed, mind the different scale) 0.01Pt-SiO_2/ZSM-22.

smaller particles and because they were mainly present in samples with higher weight loadings, their overall impact on the n_{Pt}/n_A ratios is limited. Furthermore, the textural properties of the zeolite-binder mixtures, also when Pt was included, were all very alike as observed with N_2-physisorption (Table S2). The bifunctional catalysts therefore differ in platinum particle location and platinum weight loading, whereas the acidic properties are similar in all cases.

3.3. X-ray absorption spectroscopy to study the nature of Pt sites

X-ray absorption spectroscopy was performed in order to obtain more information on the nature of the Pt sites after reduction. Linear Combination Fitting (LCF) of the Pt L_3 edge X-ray absorption near edge structure (XANES, Fig. S1) was used to determine the average Pt oxidation state for the various catalysts (Table 2).

Interestingly, the XANES LCF results of the Pt-on-SiO_2 catalysts all show that the Pt was predominantly present as Pt^0 (Table 2), unlike that of the Pt-on-Al_2O_3 catalysts prepared previously [24]. This is in

Table 2
Quantification from XANES Linear Combination Fitting (LCF) and corresponding R_{factor}.

Sample	Pt^0 (%)	Pt^{4+} (%)	R_{factor}
0.1Pt-SiO_2/ZSM-22	100	0	0.0007
0.05Pt-SiO_2/ZSM-22	93.2 ± 2.2	6.8 ± 2.2	0.014
0.01Pt-SiO_2/ZSM-22	97.6 ± 0.8	2.4 ± 0.8	0.0077
0.1Pt-ZSM-22/SiO_2	95.1 ± 1.8	4.9 ± 1.8	0.0088
0.05Pt-ZSM-22/SiO_2	95.7 ± 1.0	4.3 ± 1.0	0.0035
0.01Pt-ZSM-22/SiO_2	88.7 ± 3.9	11.3 ± 3.9	0.037
0.005Pt-ZSM-22/SiO_2	87.0 ± 4.2	13.0 ± 4.2	0.043

agreement with the fact that silica supported nanoparticles are more readily reduced than similar particles supported on alumina [41,42]. Also for the samples with Pt on ZSM-22, the majority of Pt is zero-valent. In particular for the ZSM-22 series, decreasing the metal loading led to an increase in Pt^{4+} in these samples.

Based on the Extended X-ray Absorption Fine Structure (EXAFS) in Fig. 2, qualitative information about the average local environment of the absorbing Pt atoms was derived.

When Pt was deposited on silica, both Pt-Pt (scattering paths at 2.4 and 2.9 Å) and Pt-O (scattering path below 2.0 Å) scattering [24,47] were observed at a weight loading of 0.1 wt%. At a loading of 0.05 wt%, Pt-Pt scattering became less apparent and a greater magnitude of Pt-O scattering was observed. This is in line with the results obtained with Linear Combination Fitting (Table 2) of the XANES (Fig. S2), showing that increased amounts of Pt^{4+} are present when decreasing the weight loading from 0.1 to 0.05 wt%. Decreasing the Pt weight loading to 0.01 wt% resulted in the absence of clear similarity with the reference spectra, and only a scattering path at a radial distance of 2.1 Å was observed. This could be indicative for the presence of Pt dimers [48], a hypothesis which is supported by the presence of small Pt clusters and low density of Pt nanoparticles in this sample (Fig. 1f).

Strong Pt-Pt scattering was observed for all catalysts with Pt on ZSM-22, regardless of the weight loading, proving the presence of metallic Pt nanoparticles in all of these catalysts, which can be seen in the HAADF-STEM images (Fig. 1a, c, e). At loadings <0.05 wt%, a Pt-O scattering was observed, which can indicate covalently bound oxygen, or the interaction of Pt^0 with support oxygen, or a combination thereof [49,50]. This is likely a result of the presence of small clusters or even some single atoms of Pt.

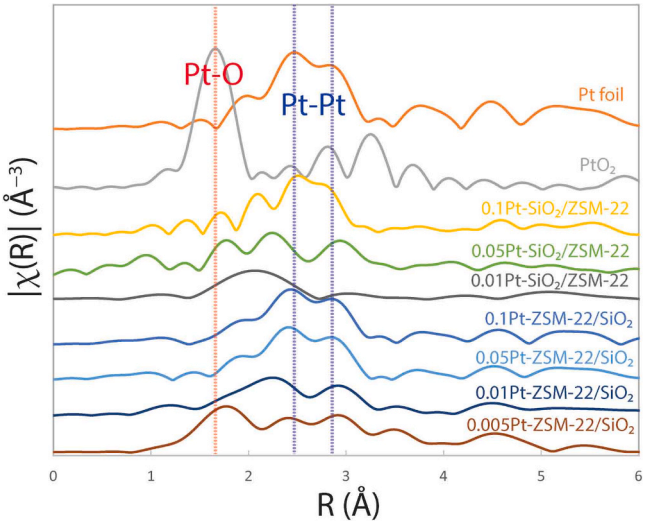

Fig. 2. Fourier Transforms of Pt L_3 edge EXAFS spectra in R space of reduced bifunctional catalysts with different Pt weight loadings and Pt nanoparticle locations.

3.4. Catalytic performance in n-heptane hydroconversion

The performance of all Pt/SiO_2/ZSM-22 catalysts for the hydroconversion of *n*-heptane is summarized in Fig. 3 and Fig. S3. At 330 °C the *n*-heptane conversion in all cases was higher at higher Pt weight loadings. The selectivity towards isomers, however, displayed a maximum with Pt loading, also when the catalysts were compared at the same conversion level. At weight loadings of 0.1 wt% or higher it was beneficial to the isomer selectivity to have the Pt nanoparticles on the binder, in line with previous research [19,25–27]. At a weight loading of 0.01 wt% or lower, placing the Pt on the silica greatly lowered the selectivity and conversion, whereas Pt-ZSM-22/SiO_2 maintained reasonable activity and even outperformed its Pt-on-SiO_2 counterpart in terms of isomer selectivity. Most likely this is caused by the shortage of Pt nanoparticles in 0.01Pt-SiO_2/ZSM-22, as evidenced by the low density of metal nanoparticles in HAADF-STEM images and absence of Pt-Pt scattering in EXAFS, and not by the chemical state of the Pt as inferred from XANES. On the contrary, the 0.01Pt-ZSM-22/SiO_2 catalysts contained a sufficient number of Pt nanoparticles to balance (de)hydrogenation with the acid-catalyzed isomerization and cracking.

For the production of dibranched isomers of *n*-heptane, it was beneficial to place Pt on the binder. This can be rationalized by shape selectivity of the zeolite and very low inward diffusivity of bulky hydrocarbons inside of the 10 MR zeolites. In Pt-SiO_2/ZSM-22 the dibranched intermediates were likely formed in the pore mouth [51–53], allowing for enhanced outward diffusion to the metal sites, preventing cracking. In other words, when formed too deep inside the zeolite pores, these intermediates cannot diffuse rapidly out of the zeolite, enhancing the formation of smaller hydrocarbons via cracking.

3.5. Catalytic performance in n-hexadecane hydroconversion and comparison with Pt/Al_2O_3/ZSM-22 catalysts

To study the effect of the location and loading of the Pt nanoparticles in Pt/SiO_2/ZSM-22 in more detail, their catalytic performance was also assessed using *n*-hexadecane as a feedstock. Furthermore, the effect of the silica binder was investigated by comparing the results to those obtained with Pt/Al_2O_3/ZSM-22 catalysts prepared previously [24]. In general, the conversion of *n*-hexadecane requires lower temperatures than the conversion of *n*-heptane when the metal loading is sufficient (Fig. S3 and S4), which is a result of the enhanced adsorption of the heavier molecule onto the catalyst. In Fig. 4 the temperature to reach 50% *n*-hexadecane conversion (T_{50}) is shown as a function of Pt weight loading. These T_{50} values were acquired by interpolation of *n*-hexadecane conversions as function of the temperature (Fig. S4).

When Pt was on the binder (either silica or alumina), the T_{50} of the low loaded catalysts was significantly higher than the T_{50} for catalysts with higher Pt loadings. When Pt was on the ZSM-22, the T_{50} does not further decrease at loadings higher than 0.01 wt% (Fig. 4). This finding is in line with what was observed with *n*-heptane hydroconversion, where Pt loadings of 0.01 wt% were sufficient to maintain catalytic activity, when the Pt was located on the ZSM-22 (Fig. 3 and ref. [24]).

The type of binder and/or support also seems to play a key role in the hydroconversion activity of catalysts with low loadings. When Pt was located on the silica, the T_{50} increased and the activity of the catalyst was drastically lower when the Pt loading was lowered from 0.5 wt% to 0.05 wt% (Fig. S4). Contrary to this, the 0.05Pt-Al_2O_3/ZSM-22 had a T_{50} that is comparable to that of the 0.5Pt-Al_2O_3/ZSM-22 catalyst in terms of activity (Fig. 4). Since n_{Pt}/n_A ratios for the SiO_2 and Al_2O_3 catalysts were similar, the cause of this difference should be ascribed to another phenomenon. A possible explanation is that, although oxidized to an extent, the XAS of 0.01Pt-Al_2O_3/ZSM-22 catalyst showed Pt-Pt scattering and in HAADF-STEM the Pt particles were clearly present. Conversely, the 0.01Pt-SiO_2/ZSM-22 catalyst exhibited no clear Pt-Pt scattering with very few Pt particles present in the HAADF-STEM images acquired. The combination of the very high dispersion and very low loading of Pt can

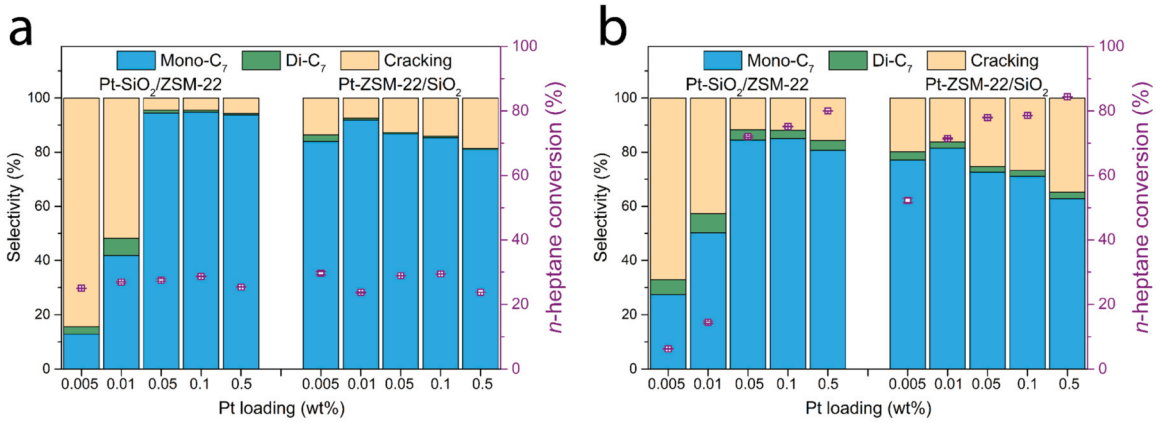

Fig. 3. Hydroconversion of *n*-heptane over Pt/SiO_2/ZSM-22 bifunctional catalysts with different Pt loadings and locations at (a) similar conversion levels of 24–30% and (b) at the same temperature of 330 °C. Reaction conditions: P = 10 bar, H_2/*n*-C_7 = 10/1 mol/mol, and WHSV = 2.5 $g_{n\text{-}C7}\cdot g_{cat}^{-1}\cdot h^{-1}$. Mono-$C_7$ indicates mono-branched *i*-heptane, Di-C_7 indicates dibranched *i*-heptane, and Cracking indicates the products that have fewer than 7 carbon atoms in their molecular structure. Error bars indicate standard deviations.

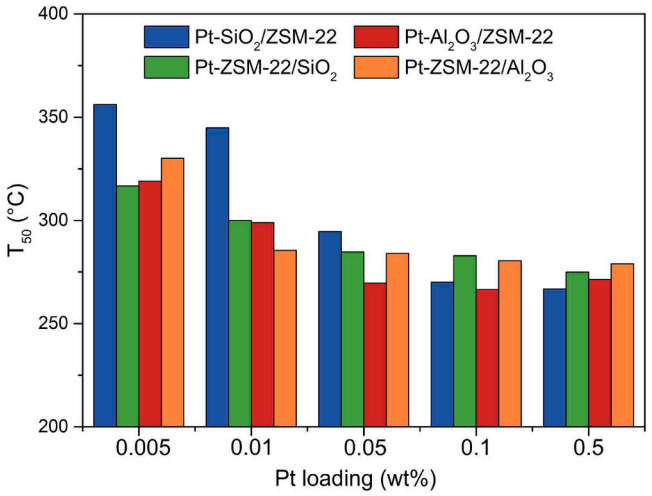

Fig. 4. Temperature to reach 50% *n*-hexadecane conversion as function of the Pt weight loading of Pt-SiO_2/ZSM-22 (blue), Pt-ZSM-22/SiO_2 (green), Pt-Al_2O_3/ZSM-22 (red), and Pt-ZSM-22/Al_2O_3 (orange) catalysts.

explain the low activity. This, in turn, also leads to a decrease in isomer selectivity at lower conversion levels and maximum isomer yield (Fig. 5, Fig. S5).

In Fig. 5a and b the selectivity of the catalysts at a conversion level of 20–32% is compared. At these conversion levels, catalysts with low Pt loadings (≤0.01 wt%) on a silica or alumina binder displayed poor isomer selectivities compared to most of their counterparts in which the Pt was placed on/in ZSM-22. Therefore, at low loadings and at relatively low conversion levels (20–32%) it was typically beneficial for the isomer selectivity to have the Pt deposited on the zeolite.

Nevertheless, maximum yields (attained at different temperatures, Table S3) of branched hexadecane (Fig. 5c,d) required relatively high weight loadings of ≥0.1 wt% with Pt on the binder. When alumina was used as binder, a Pt weight loading of 0.05 wt% (Fig. 5b) did not significantly compromise the isomer yield compared to higher loadings. At lower loadings (<0.05 wt%), however, it was beneficial to have the Pt on ZSM-22. Generally speaking, catalysts with Pt on ZSM-22 maintained relatively high isomer yields when the Pt weight loading was decreased. When Pt was on the binder, particularly on SiO_2, low Pt loadings were detrimental to the isomer yield. In combination with the decreased activity of Pt-on-binder catalysts with low loadings with respect to the Pt-on-ZSM-22 catalysts (Fig. 4), it is concluded that it is beneficial to locate Pt on the zeolite when ultralow (≤0.01 wt%) loadings of Pt are used. In terms of overall catalytic performance, a loading of 0.05 wt% or higher was required to sustain decent catalytic performance. This is a higher weight loading than for the *n*-heptane hydroconversion reaction, which is in line with the fact that generally higher n_{Pt}/n_A ratios are required for adequate catalytic performance during the hydroconversion of longer hydrocarbons [29]. However, the experiments with the *n*-hexadecane feedstock were conducted at a total pressure of 5 bar, whereas *n*-heptane hydroconversion experiments were performed at 10 bar. Both the heavier hydrocarbon feedstock and the lower hydrogen partial pressure with hexadecane experiments are expected to increase the required metal loading [29,54] and the effects could not be disentangled based on these experiments.

Looking at the catalysts with Pt loadings ≥0.05 wt% for the alumina binder and ≥0.1 wt% for the silica binder, it was preferred to keep the Pt located on the binder. This can be rationalized by the lower diffusivities of longer and bulkier hydrocarbons within the zeolite micropores [51–53,55]. Decreasing the n_{Pt}/n_A ratio resulted in catalysts that favored overcracking of the feedstock (Fig. S6) and the carbon distribution started to deviate substantially from a distribution that would be obtained during "ideal" hydrocracking [56]. The minimum Pt weight loading and preferred nanoparticle location in bifunctional metal-acid catalysts are affected by both the process conditions and the molecular weight of the hydrocarbon feedstock.

4. Conclusions

A set of Pt/SiO_2/ZSM-22 catalysts with differing Pt weight loadings and nanoparticle locations were prepared and characterized. Pt weight loadings of 0.01 wt% and lower led to fewer visible Pt nanoparticles (HR HAADF-STEM) and limited Pt-Pt coordination (XAS) when located on the silica binder, while at the same loading of Pt on the ZSM-22, the catalysts had abundant observable Pt nanoparticles. Their catalytic performance during the hydroconversion of *n*-heptane was assessed and at low loadings (0.01 wt%) the catalytic activity and selectivity benefited from Pt being present on the ZSM-22 crystals, which is likely a result of the presence of Pt nanoparticles in sufficient numbers at that location. The hydroconversion of longer-chain hydrocarbons (*n*-hexadecane) over catalysts with ultralow amounts of Pt at different locations was assessed for the first time and the performance of Pt/SiO_2/ZSM-22 catalysts was compared to that of Pt/Al_2O_3/ZSM-22 catalysts. For the hydroconversion of *n*-hexadecane a Pt weight loading of ≥0.05 wt%, preferentially placed on the binder, was desired. Decreasing the Pt loading led to a decrease in catalytic activity, regardless of the Pt location. Pt-on-SiO_2 catalysts displayed very low activity at loadings of

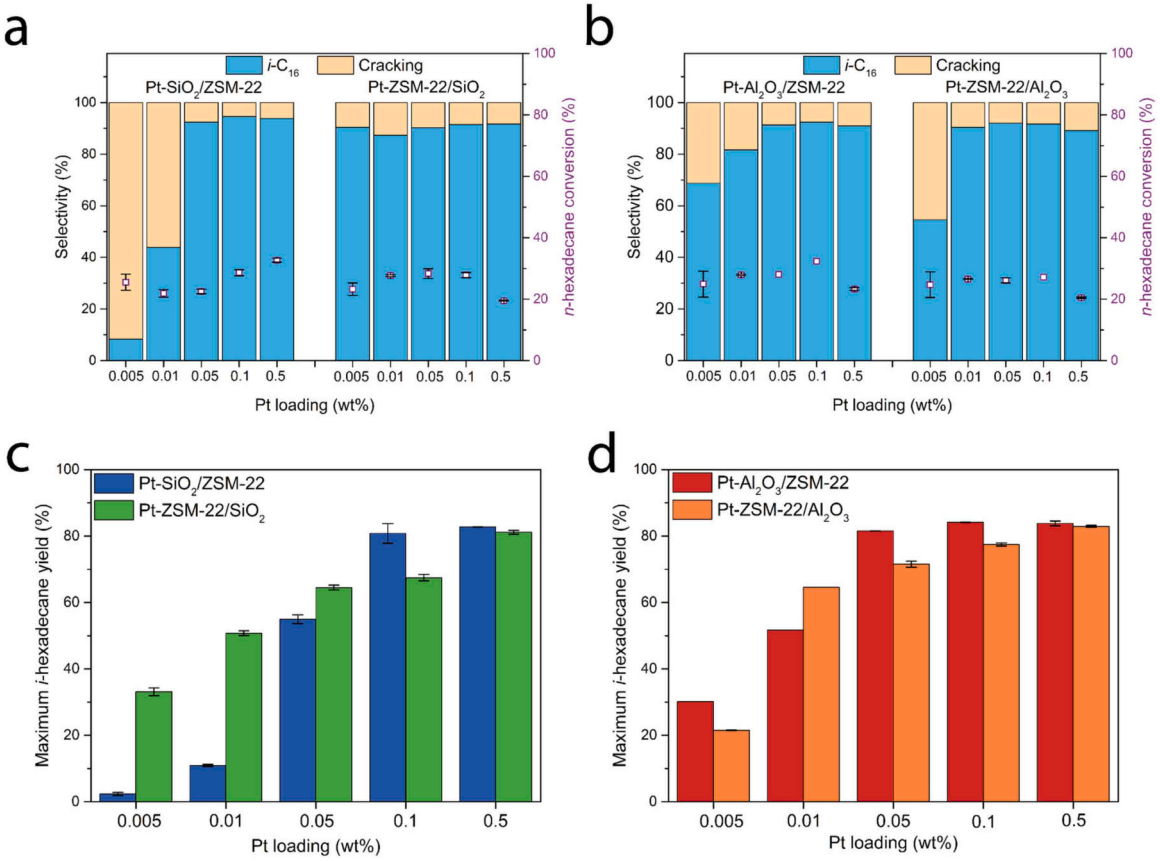

Fig. 5. (a) $Pt/SiO_2/ZSM-22$ catalyst selectivity during *n*-hexadecane conversion at similar conversion levels (20–32%), (b) $Pt/Al_2O_3/ZSM-22$ catalyst selectivity during *n*-hexadecane conversion at similar conversion levels (20–32%), and maximum *i*-hexadecane yields obtained with (c) $Pt/SiO_2/ZSM-22$ catalysts and (d) $Pt/Al_2O_3/ZSM-22$ catalysts as function of the Pt loading. Reaction conditions: P = 5 bar, $H_2/n\text{-}C_{16}$ = 10/1 mol/mol, and WHSV = 2.9 $g_{n\text{-}C16} \cdot g_{cat}^{-1} \cdot h^{-1}$. Error bars indicate standard deviations.

0.01 wt% or lower, whereas Pt-on-Al_2O_3 catalysts still show activity and selectivity at these loadings. Based on the XAS and STEM results for 0.01Pt-SiO_2/ZSM-22 catalysts, although predominantly present as Pt^0, the Pt dispersion appeared to be too high and the loading too low on these catalysts leading to a poor catalytic performance. Silica therefore was not a better binder and support for bifunctional hydroconversion catalysts with ultralow platinum loadings.

CRediT authorship contribution statement

Luc C.J.Smulders: Conceptualization, Formal analysis, Investigation, Methodology, Project administration, Validation, Visualization, Writing – original draft, Writing – review & editing. **Arvid J. Beeuwkes:** Formal analysis, Investigation, Methodology, Validation, Writing – review & editing. **Kang Cheng:** Formal analysis, Investigation, Methodology, Validation, Writing – review & editing. **Johannes D. Meeldijk:** Investigation, Writing – review & editing. **Zhuoran Xu:** Formal analysis, Investigation, Writing – review & editing. **George F. Tierney:** Formal analysis, Writing – review & editing. **Eric Doskocil:** Conceptualization, Writing – review & editing. **S. Tegan Roberts:** Conceptualization, Writing – review & editing. **Glenn J. Sunley:** Conceptualization, Writing – review & editing. **Petra E. de Jongh:** Conceptualization, Funding acquisition, Resources, Supervision, Writing – review & editing. **Krijn P. de Jong:** Conceptualization, Funding acquisition, Methodology, Project administration, Resources, Supervision, Writing – review & editing.

Declaration of Competing Interest

The authors declare that they have no known competing financial interests or personal relationships that could have appeared to influence the work reported in this paper.

Data availability

Data will be made available on request.

Acknowledgments

The authors thank Dennie Wezendonk, Jan Willem de Rijk and Remco Dalebout for their help commissioning the Flowrence setup. Tom Welling and Karan Kotalgi are thanked for performing the N_2 physisorption measurements. This research was funded by BP plc, United Kingdom.

Appendix A. Supporting information

Supplementary data associated with this article can be found in the online version at doi:10.1016/j.cattod.2024.114508.

References

[1] L. Chong, J. Wen, J. Kubal, F.G. Sen, J. Zou, J. Greeley, M. Chan, H. Barkholtz, W. Ding, D.J. Liu, Ultralow-loading platinum-cobalt fuel cell catalysts derived from imidazolate frameworks, Science 362 (2018) 1276–1281, https://doi.org/10.1126/science.aau0630.

[2] G. Reverdiau, A. Le Duigou, T. Alleau, T. Aribart, C. Dugast, T. Priem, Will there be enough platinum for a large deployment of fuel cell electric vehicles? Int. J.

Hydrog. Energy 46 (2021) 39195–39207, https://doi.org/10.1016/j.ijhydene.2021.09.149.
[3] M.C.O. Monteiro, A. Goyal, P. Moerland, M.T.M. Koper, Understanding cation trends for hydrogen evolution on platinum and gold electrodes in alkaline media, ACS Catal. 11 (2021) 14328–14335, https://doi.org/10.1021/acscatal.1c04268.
[4] E. Kritsanaviparkporn, F.M. Baena-Moreno, T.R. Reina, Catalytic converters for vehicle exhaust: fundamental aspects and technology overview for newcomers to the field, Chem 3 (2021) 630–646, https://doi.org/10.3390/chemistry3020044.
[5] P. Mäki-Arvela, T.A.K. Khel, M. Azkaar, S. Engblom, D.Y. Murzin, Catalytic hydroisomerization of long-chain hydrocarbons for the production of fuels, Catalysts 8 (2018), https://doi.org/10.3390/catal8110534.
[6] S. Bobba, S. Carrara, J. Huisman, F. Mathieux, C. Pavel, Critical raw materials for strategic technologies and sectors in the EU - a foresight study, Publ (2020), https://doi.org/10.2873/58081.
[7] A.E. Hughes, N. Haque, S.A. Northey, S. Giddey, Platinum group metals: a review of resources, production and usage with a focus on catalysts, Resources 10 (2021) 1–40, https://doi.org/10.3390/resources10090093.
[8] W. Böhringer, A. Kotsiopoulos, M. de Boer, C. Knottenbelt, J.C.Q. Fletcher, Selective Fischer–Tropsch wax hydrocracking - opportunity for improvement of overall gas-to-liquids processing, Stud. Surf. Sci. Catal. 163 (2007) 345–365, https://doi.org/10.1016/S0167-2991(07)80488-5.
[9] C. Bouchy, G. Hastoy, E. Guillon, J.A. Martens, Fischer–Tropsch waxes upgrading via hydrocracking and selective hydroisomerization, Oil Gas. Sci. Technol. 64 (2009) 91–112, https://doi.org/10.2516/ogst/2008047.
[10] P. Mäki-Arvela, M. Martínez-Klimov, D.Y. Murzin, Hydroconversion of fatty acids and vegetable oils for production of jet fuels, Fuel 306 (2021), https://doi.org/10.1016/j.fuel.2021.121673.
[11] P.A. Kots, B.C. Vance, D.G. Vlachos, Polyolefin plastic waste hydroconversion to fuels, lubricants, and waxes: a comparative study, React. Chem. Eng. 7 (2022) 41–54, https://doi.org/10.1039/d1re00447f.
[12] J.E. Rorrer, A.M. Ebrahim, Y. Questell-Santiago, J. Zhu, C. Troyano-Valls, A. S. Asundi, A.E. Brenner, S.R. Bare, C.J. Tassone, G.T. Beckham, Y. Román-Leshkov, Role of bifunctional Ru/acid catalysts in the selective hydrocracking of polyethylene and polypropylene waste to liquid hydrocarbons, ACS Catal. 12 (2022) 13969–13979, https://doi.org/10.1021/acscatal.2c03596.
[13] W.T. Lee, A. van Muyden, F.D. Bobbink, M.D. Mensi, J.R. Carullo, P.J. Dyson, Mechanistic classification and benchmarking of polyolefin depolymerization over silica-alumina-based catalysts, Nat. Commun. 13 (2022) 1–13, https://doi.org/10.1038/s41467-022-32563-y.
[14] A. Corma, Transformation of hydrocarbons on zeolite catalysts, Catal. Lett. 22 (1993) 33–52, https://doi.org/10.1007/BF00811768.
[15] E.T.C. Vogt, G.T. Whiting, A. Dutta Chowdhury, B.M. Weckhuysen, Zeolites and zeotypes for oil and gas conversion, Adv. Catal. 58 (2015) 143–314, https://doi.org/10.1016/bs.acat.2015.10.001.
[16] W. Wang, C.-J. Liu, W. Wu, Bifunctional catalysts for the hydroisomerization of n-alkanes: the effects of metal–acid balance and textural structure, Catal. Sci. Technol. 9 (2019) 4162–4187, https://doi.org/10.1039/C9CY00499H.
[17] P.B. Weisz, Stepwise reaction via intermediates on separate catalytic centers, Science 123 (1956) 887–888, https://doi.org/10.1126/science.123.3203.887.
[18] P.B. Weisz, E.W. Swegler, Stepwise reaction on separate catalytic centers: isomerization of saturated hydrocarbons, Science 126 (1957) 31–32, https://doi.org/10.1126/science.126.3262.31.
[19] J. Zecevic, G. Vanbutsele, K.P. de Jong, J.A. Martens, Nanoscale intimacy in bifunctional catalysts for selective conversion of hydrocarbons, Nature 528 (2015) 245–254, https://doi.org/10.1038/nature16173.
[20] N. Batalha, L. Pinard, C. Bouchy, E. Guillon, M. Guisnet, N-Hexadecane hydroisomerization over Pt-HBEA catalysts. quantification and effect of the intimacy between metal and protonic sites, J. Catal. 307 (2013) 122–131, https://doi.org/10.1016/j.jcat.2013.07.014.
[21] M. Guisnet, F. Alvarez, G. Giannetto, G. Perot, Hydroisomerization and hydrocracking of n-heptane on PtH zeolites. Effect of the porosity and of the distribution of metallic and acid sites, Catal. Today 1 (1987) 415–433, https://doi.org/10.1016/0920-5861(87)80007-X.
[22] F. Alvarez, F.R. Ribeiro, G. Perot, C. Thomazeau, M. Guisnet, Hydroisomerization and hydrocracking of alkanes, J. Catal. 162 (1996) 179–189, https://doi.org/10.1006/jcat.1996.0275.
[23] J.I. Mirena, J.W. Thybaut, G.B. Marin, J.A. Martens, V.V. Galvita, Impact of the spatial distribution of active material on bifunctional hydrocracking, Ind. Eng. Chem. Res. (2021), https://doi.org/10.1021/acs.iecr.0c05528.
[24] K. Cheng, L.C.J. Smulders, L.I. van der Wal, J. Oenema, J.D. Meeldijk, N.L. Visser, G. Sunley, T. Roberts, Z. Xu, E. Doskocil, H. Yoshida, Y. Zheng, J. Zečević, P.E. de Jongh, K.P. de Jong, Maximizing noble metal utilization in solid catalysts by control of nanoparticle location, Science 377 (2022) 204–208, https://doi.org/10.1126/science.abn8289.
[25] J. Oenema, J.P. Hofmann, E.J.M. Hensen, J. Zečević, K.P. de Jong, Assessment of the location of Pt nanoparticles in Pt/zeolite Y/γ-Al2O3 composite catalysts, ChemCatChem 12 (2020) 615–622, https://doi.org/10.1002/cctc.201901617.
[26] K. Cheng, L.I. van der Wal, H. Yoshida, J. Oenema, J. Harmel, Z. Zhang, G. Sunley, J. Zečević, K.P. de Jong, Impact of the spatial organization of bifunctional metal–zeolite catalysts on the hydroisomerization of light alkanes, Angew. Chem. Int. Ed. 59 (2020) 3592–3600, https://doi.org/10.1002/anie.201915080.
[27] L.C.J. Smulders, J.H. van de Minkelis, J.D. Meeldijk, M. Tang, A. Liutkova, K. Cheng, S.T. Roberts, G.J. Sunley, E.J.M. Hensen, P.E. de Jongh, K.P. de Jong, Steering the metal precursor location in Pd/zeotype catalysts and its implications for catalysis, Chemistry 5 (2023) 348–364, https://doi.org/10.3390/chemistry5010026.
[28] L.I. van der Wal, J. Oenema, L.C.J. Smulders, N.J. Samplonius, K.R. Nandpersad, J. Zečević, K.P. de Jong, Control and Impact of metal loading heterogeneities at the nanoscale on the performance of Pt/Zeolite Y catalysts for alkane hydroconversion, ACS Catal. 11 (2021) 3842–3855, https://doi.org/10.1021/acscatal.1c00211.
[29] C. Wei, G. Zhang, L. Zhao, J. Gao, C. Xu, Effect of metal–acid balance and textual modifications on hydroisomerization catalysts for n-alkanes with different chain length: a mini-review, Fuel 315 (2022) 122809, https://doi.org/10.1016/j.fuel.2021.122809.
[30] J. Weitkamp, Isomerization of long-chain n-alkanes on a Pt/CaY zeolite catalyst, Ind. Eng. Chem. Prod. Res. Dev. 21 (1982) 550–558, https://doi.org/10.1021/i300008a008.
[31] J. Weitkamp, The influence of chain length in hydrocracking and hydroisomerization of n -alkanes, Am. Chem. Soc. Div. Pet. Chem. Prepr. (1975) 1–27, https://doi.org/10.1021/bk-1975-0020.ch001.
[32] K.Y. Lee, H.K. Lee, S.K. Ihm, Influence of catalyst binders on the acidity and catalytic performance of HZSM-5 zeolites for methanol-to-propylene (MTP) process: single and binary binder system, Top. Catal. 53 (2010) 247–253, https://doi.org/10.1007/s11244-009-9412-0.
[33] N.L. Michels, S. Mitchell, J. Pérez-Ramírez, Effects of binders on the performance of shaped hierarchical MFI zeolites in methanol-to-hydrocarbons, ACS Catal. 4 (2014) 2409–2417, https://doi.org/10.1021/cs500353b.
[34] R. Bingre, B. Louis, P. Nguyen, An overview on zeolite shaping technology and solutions to overcome diffusion limitations, Catalysts 8 (2018), https://doi.org/10.3390/catal8040163.
[35] Z. Asgar Pour, M.M. Abduljawad, Y.A. Alassmy, L. Cardon, P.H.M. Van Steenberge, K.O. Sebakhy, A comparative review of binder-containing extrusion and alternative shaping techniques for structuring of zeolites into different geometrical bodies, Catalysts 13 (2023) 656, https://doi.org/10.3390/catal13040656.
[36] Z. Vajglová, N. Kumar, P. Mäki-Arvela, K. Eränen, M. Peurla, L. Hupa, D.Y. Murzin, Effect of binders on the physicochemical and catalytic properties of extrudate-shaped beta zeolite catalysts for cyclization of citronellal, Org. Process Res. Dev. 23 (2019) 2456–2463, https://doi.org/10.1021/acs.oprd.9b00346.
[37] S. Mitchell, N.L. Michels, J. Pérez-Ramírez, From powder to technical body: the undervalued science of catalyst scale up, Chem. Soc. Rev. 42 (2013) 6094–6112, https://doi.org/10.1039/c3cs60076a.
[38] G.T. Whiting, F. Meirer, M.M. Mertens, A.J. Bons, B.M. Weiss, P.A. Stevens, E. De Smit, B.M. Weckhuysen, Binder effects in SiO2- and Al2O3-bound zeolite ZSM-5-based extrudates as studied by microspectroscopy, ChemCatChem 7 (2015) 1312–1321, https://doi.org/10.1002/cctc.201402897.
[39] K. Yang, D. Zhang, M. Zou, L. Yu, S. Huang, The known and overlooked sides of zeolite-extrudate catalysts, ChemCatChem 13 (2021) 1414–1423, https://doi.org/10.1002/cctc.202001601.
[40] S. Guo, S. Yu, H. Tian, Z. Da, Mechanistic insights into the interaction between binders and Y-type zeolites in fluid catalytic cracking, Fuel 324 (2022), https://doi.org/10.1016/j.fuel.2022.124640.
[41] O.A. Bariås, A. Holmen, E.A. Blekkan, Propane dehydrogenation over supported Pt and Pt-Sn catalysts: catalyst preparation, characterization, and activity measurements, J. Catal. 158 (1996) 1–12, https://doi.org/10.1006/jcat.1996.0001.
[42] S. Penner, D. Wang, D.S. Su, G. Rupprechter, R. Podloucky, R. Schlögl, K. Hayek, Platinum nanocrystals supported by silica, alumina and ceria: Metal-support interaction due to high-temperature reduction in hydrogen, Surf. Sci. 532–535 (2003) 276–280, https://doi.org/10.1016/S0039-6028(03)00198-5.
[43] H.R. Cho, J.R. Regalbuto, The rational synthesis of Pt-Pd bimetallic catalysts by electrostatic adsorption, Catal. Today 246 (2015) 143–153, https://doi.org/10.1016/j.cattod.2014.09.029.
[44] M. Newville, EXAFS analysis using FEFF and FEFFIT, J. Synchrotron Radiat. 8 (2001) 96–100, https://doi.org/10.1107/S0909049500016290.
[45] B. Ravel, M. Newville, ATHENA, ARTEMIS, HEPHAESTUS: data analysis for X-ray absorption spectroscopy using IFEFFIT, J. Synchrotron Radiat. 12 (2005) 537–541, https://doi.org/10.1107/S0909049505012719.
[46] J. Kim, W. Kim, Y. Seo, J.C. Kim, R. Ryoo, N-Heptane hydroisomerization over Pt/MFI zeolite nanosheets: effects of zeolite crystal thickness and platinum location, J. Catal. 301 (2013) 187–197, https://doi.org/10.1016/j.jcat.2013.02.015.
[47] H. Jeong, O. Kwon, B.S. Kim, J. Bae, S. Shin, H.E. Kim, J. Kim, H. Lee, Highly durable metal ensemble catalysts with full dispersion for automotive applications beyond single-atom catalysts, Nat. Catal. 3 (2020) 368–375, https://doi.org/10.1038/s41929-020-0427-z.
[48] U. Müller, K. Sattler, J. Xhie, N. Venkateswaran, G. Raina, A scanning tunneling microscope study of single platinum atoms, platinum dimers and trimers on highly-oriented pyrolytic graphite, Z. Phys. D Mol. Clust. 19 (1991) 319–321, https://doi.org/10.1007/BF01448320.
[49] M. Vaarkamp, F.S. Modica, J.T. Miller, D.C. Koningsberger, Influence of hydrogen pretreatment on the structure of the metal-support interface in Pt/zeolite catalysts, J. Catal. 144 (1993) 611–626, https://doi.org/10.1006/jcat.1993.1357.
[50] J. Finzel, K.M. Sanroman Gutierrez, A.S. Hoffman, J. Resasco, P. Christopher, S. R. Bare, Limits of detection for EXAFS characterization of heterogeneous single-atom catalysts, ACS Catal. 13 (2023) 6462–6473, https://doi.org/10.1021/acscatal.3c01116.
[51] J.A. Martens, W. Souverijns, W. Verrelst, R. Parton, G.F. Froment, P.A. Jacobs, Selective isomerization of hydrocarbon chains on external surfaces of zeolite crystals, Angew. Chem. Int. Ed. Engl. 34 (1995) 2528–2530, https://doi.org/10.1002/anie.199525281.
[52] J.A. Martens, G. Vanbutsele, P.A. Jacobs, J. Denayer, R. Ocakoglu, G. Baron, J. A. Muñoz Arroyo, J. Thybaut, G.B. Marin, Evidences for pore mouth and key-lock catalysis in hydroisomerization of long n-alkanes over 10-ring tubular pore

bifunctional zeolites, Catal. Today 65 (2001) 111–116, https://doi.org/10.1016/S0920-5861(00)00577-0.
[53] C. Chizallet, C. Bouchy, K. Larmier, G. Pirngruber, Molecular views on mechanisms of brønsted acid-catalyzed reactions in zeolites, Chem. Rev. 123 (2023) 6107–6196, https://doi.org/10.1021/acs.chemrev.2c00896.
[54] J.W. Thybaut, C.S. Laxmi Narasimhan, J.F. Denayer, G.V. Baron, P.A. Jacobs, J. A. Martens, G.B. Marin, Acid-metal balance of a hydrocracking catalyst: ideal versus nonideal behavior, Ind. Eng. Chem. Res. 44 (2005) 5159–5169, https://doi.org/10.1021/ie049375.
[55] G. Noh, S.I. Zones, E. Iglesia, Isomer sieving and the selective formation of terminal methyl isomers in reactions of linear alkanes on one-dimensional zeolites, J. Catal. 377 (2019) 255–270, https://doi.org/10.1016/j.jcat.2019.07.022.
[56] J. Weitkamp, Catalytic hydrocracking—mechanisms and versatility of the process, ChemCatChem 4 (2012) 292–306, https://doi.org/10.1002/cctc.201100315.